Applied Catalysis B: Environmental 321 (2023) 122082

Contents lists available at ScienceDirect

Applied Catalysis B: Environmental

journal homepage: www.elsevier.com/locate/apcatb

A MOF-on-MOF strategy to construct double Z-scheme heterojunction for high-performance photocatalytic degradation

Hassan Sepehrmansourie [a,1], Hassan Alamgholiloo [b,*,2], Nader Noroozi Pesyan [b,3], Mohammad Ali Zolfigol [a,*,4]

[a] Department of Organic Chemistry, Faculty of Chemistry, Bu-Ali Sina University, Hamedan 6517838683, Iran
[b] Department of Organic Chemistry, Faculty of Chemistry, Urmia University, 57159 Urmia, Iran

ARTICLE INFO

Keywords:
Double Z-scheme heterojunction
Ofloxacin
Photocatalytic degradation
MOF-on-MOF
Visible light irradiation

ABSTRACT

Well-organized UiO-66-on-MIL-125 growth onto g-C_3N_4 nanosheets was developed for ofloxacin (OFL) antibiotics degradation under visible light irradiation ($\lambda > 420$ nm). First, NH_2-MIL-125 as a host MOF was prepared by a solvothermal method, and then UiO-66 crystals were grown onto the NH_2-MIL-125 surface with the same method. Subsequently, g-C_3N_4 nanosheets were decorated onto Zr-MOF-on-Ti-MOF surface to obtain a new type of the double Z-scheme UiO-66/NH_2-MIL-125/g-C_3N_4 heterojunction. Under visible light irradiation, this double Z-scheme heterojunction acts as a highly efficient photocatalyst for the degradation of OFL with a rate constant of 0.07 min^{-1}, which is about 1.79 times higher than that of pristine UiO-66-on-MIL-125. Also, the findings obtained from radical trapping and EPR indicated that $^{\bullet}OH$ and $^{\bullet}O_2^-$ play an essential role in OFL photodegradation. The current study provides not only new horizons to architecture MOF on other MOFs but also develops Z-scheme heterojunction materials for removing emerging pollutants from wastewater.

1. Introduction

With the increasing population and industrialization of societies, the concentration of antibiotics in natural water and soil has far exceeded the average standards, which is a serious risk to public health and the environment [1,2]. As one of the popular antibiotics, ofloxacin (OFL) was widely used for treating bacterial infections in humans and animals [3,4]. Unfortunately, the OFL macromolecules are released into the water environment due to their poor metabolism in humans and animals, where their concentration is much higher than that of other types of antibiotics [5,6]. In addition, wastewater treatment can not completely remove these compounds from the effluent, which has a negative effect on the ecosystem balance [7]. Auspiciously, utilizing photo-based advanced oxidation processes (AOPs) is a potential platform for resolving these problems [8–11]. Among various AOP methods, semiconductor photocatalysis systems are the most widely used methods to generate reactive oxygen species (ROS) under sunlight [12,13], which has the potential to convert macromolecular organic pollutants to nontoxic and harmless products. Meanwhile, the application of sunlight as a source of green energy with high efficiency is a promising approach for antibiotic pollutants control [14,15]. Therefore, to develop the best way to use sunlight in AOPs, it seems necessary to design and fabricate a new type of Z-scheme heterojunction photocatalyst to create a safe ecosystem.

The conjugation of two or more different metal-organic frameworks (MOFs) as a new generation of complicated MOF hybrids has drawn significant interest in the development of nanomaterials architectures [16–19]. These engineered nanostructures have potential in catalytic and photocatalytic applications due to the unique properties of MOF-on-MOF in comparison to individual MOFs [20–24]. Recently, modern techniques for the architectures of MOF-on-MOF like yolk-shell [25], core-shell [26–28], film on film [29,30], and asymmetric framework [31,32] have been proposed. These nanostructures have revealed unique features and can be compensated limitations of individual MOFs

* Corresponding authors.
E-mail addresses: h.alamgholiloo@urmia.ac.ir, H.alamgholilo2013@yahoo.com (H. Alamgholiloo), mzolfigol@yahoo.com, zolfi@basu.ac.ir (M.A. Zolfigol).
[1] 0000-0002-9064-9078.
[2] 0000-0002-7058-8079.
[3] 0000-0002-4257-434X.
[4] 0000-0002-4970-8646.

https://doi.org/10.1016/j.apcatb.2022.122082
Received 17 June 2022; Received in revised form 6 October 2022; Accepted 14 October 2022
Available online 17 October 2022
0926-3373/© 2022 Elsevier B.V. All rights reserved.

[19]. Also, MOFs@MOFs composites in nanoscale can be potential disease treatment platforms [33,34]. Therefore, expanding these nanostructures can be necessary to promote public health and the environment.

Recently, Oh and colleagues have explored the isotropic growth of MIL-68-Br on MIL-68 [35], while this research team has reported tip-to-middle anisotropic growth Fe-MIL-88B@Fe-MIL-88 C for expanding architectures of MOF-on-MOF [31]. In addition to binary MOF-on-MOF systems, ternary MOF-on-MOF architecture has also been recently developed. In this regard, Yu and their co-worker have developed three types of ternary MOF-on-MOF hybrids with controllable architectural [36]. Furthermore, Kitagawa and co-workers have expanded new types of ternary MOF-on-MOF hybrids of UiO-66/-MOF-76 @MIL-125 for developing MOF-on-MOF architectures [37].

The MOF-on-MOF architecture could effectively facilitate charge separation and carrier transfer and significantly improve photocatalytic activities. In addition to porosity and stability, these hybrid nanomaterials could make sure the opposite migration of electrons and holes by conduction band (CB) and valence band (VB) [38]. This new type of hybrid nanomaterials could provide more possibilities for structural and functional modulation and better maintenance of the large surface area, intrinsic porosity, and high crystallinity [39,40]. As a class of nanoreactors, architecture MOF-on-MOFs on g-C_3N_4 sheets are promising candidates for wastewater treatment.

A significant potential advantage of nanostructures containing Ti-MOF, Zr-MOF, and g-C_3N_4 is the possibility of using sunlight to separate photogenerated electron-hole pairs [41–44], which is convenient, economical, and efficient. Concerning the above issues and our previous reports on developing engineered nanomaterials [45–53], we have explored the epitaxial growth of UiO-66 on the NH_2-MIL-125 surface via the solvothermal method for developing MOF-on-MOF architectures. Subsequently, we successfully decorate g-C_3N_4 nanosheets in UiO-66/NH_2-MIL-125 surface to design a new type of double Z-scheme heterojunction photocatalyst for degradation of OFL under visible light. According to the latest findings, there is no report on the fabrication and study of the photocatalytic properties of the proposed nanostructure with controllable architecture. These findings not only provide deep insight into the architecture of MOF-on-MOF onto layer nanomaterials but also suggest an effective strategy for the degradation of organic pollutants under visible light.

2. Materials and methods

2.1. Chemical reagents

Zirconium chloride ($ZrCl_4$, 99%), melamine ($C_3H_6N_6$, 99%), 2-amino terephthalic acid (NH_2-BDC, 95%), terephthalic acid (H_2BDC, 95%) titanium tetraisopropanolate (TTIP, 99.8%), polyvinylpyrrolidone (PVP, 99%), and *N*, *N*-dimethylformamide (DMF, 99%) were purchased from Sigma-Aldrich and Merck. Moreover, OFL antibiotic ($C_{18}H_{20}FN_3O_4$, MW: 361.1 g mol^{-1}, 98%) was bought from EXCIR-Pharmaceutical Co., Ltd (Tehran, Iran); Furthermore, ethylenediaminetetracetic acid disodium (EDTA-2Na), potassium dichromate ($K_2Cr_2O_7$) benzoquinone (BQ), tert-butanol (TBA), methanol (MeOH), and ethanol (EtOH) were purchased from Kimia-Gostar Co., Ltd (Tehran, Iran).

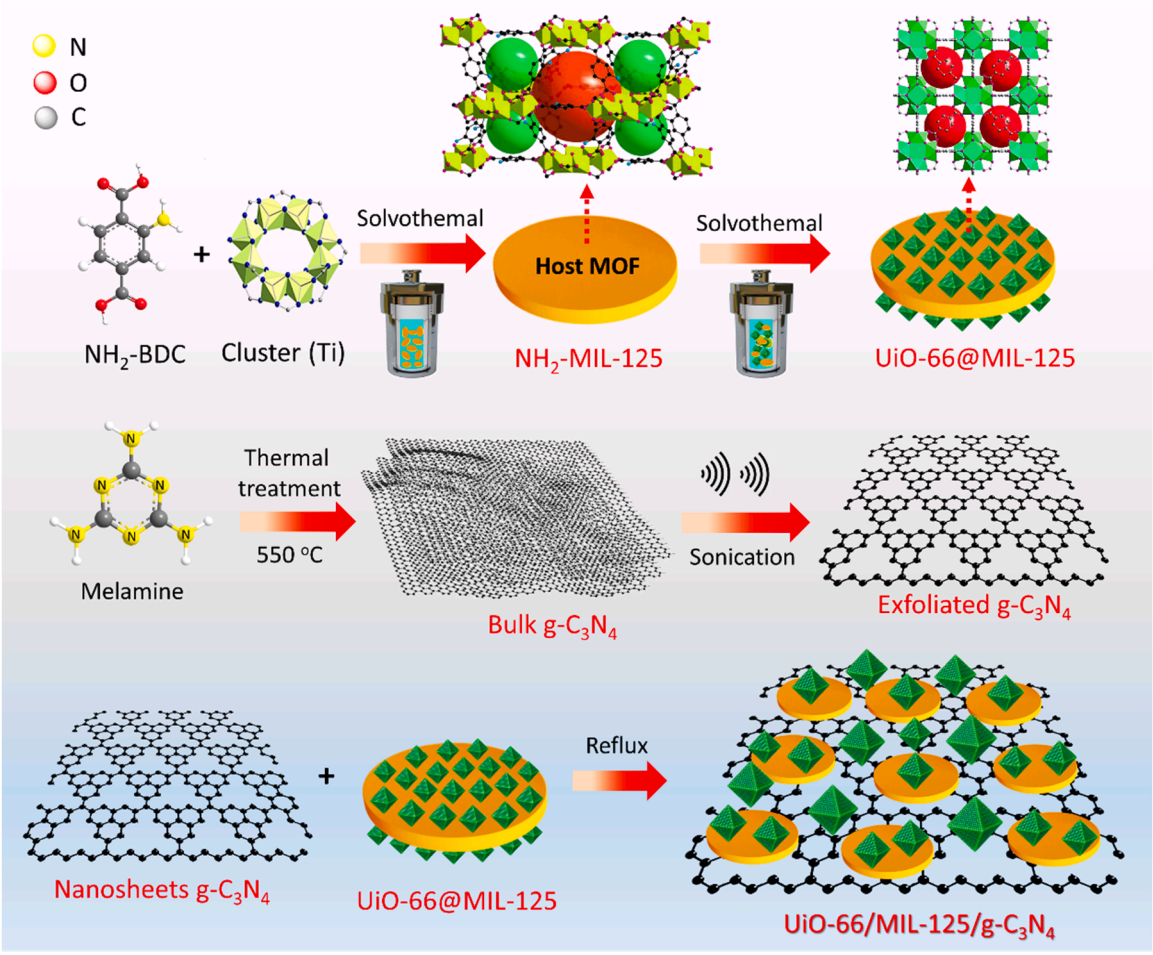


Fig. 1. Schematic representation for the fabrication of UiO/MIL/CN hybrid structure.

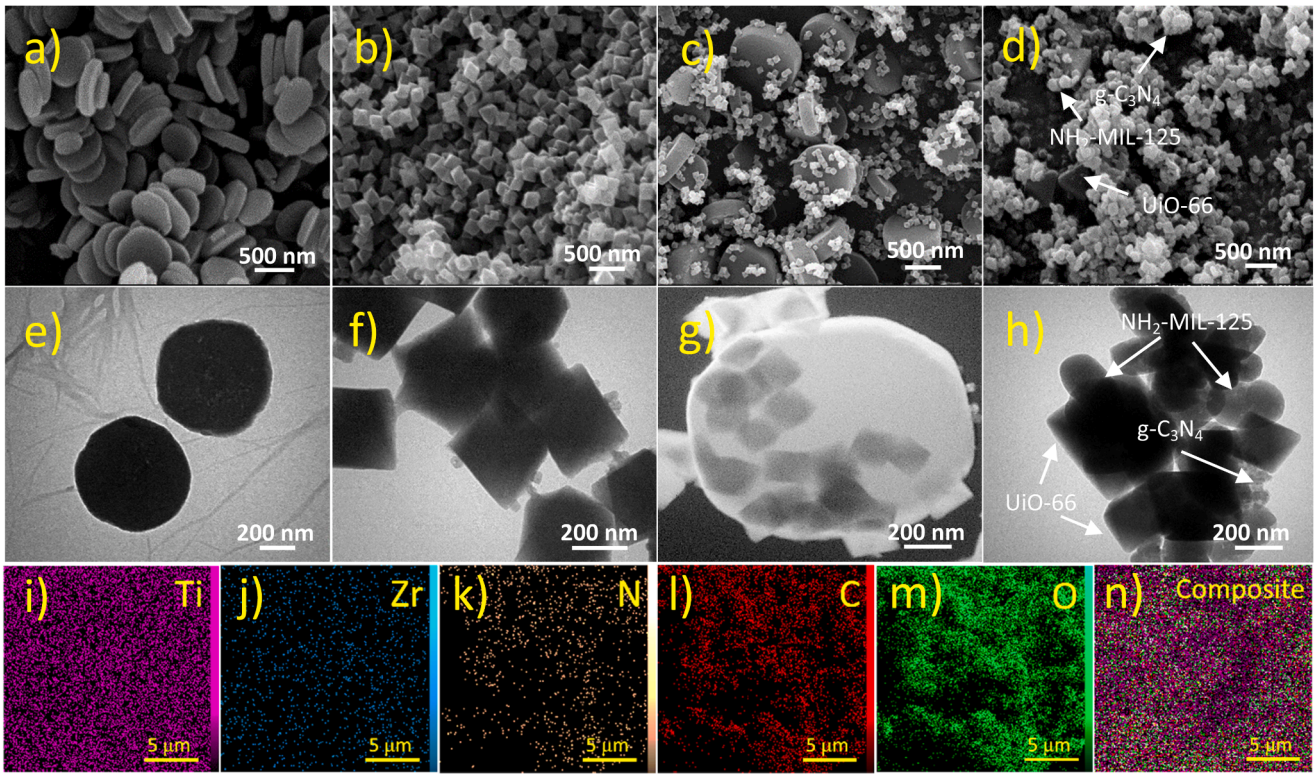


Fig. 2. FESEM images of NH_2-MIL-125 (a), UiO-66 (b), UiO-on-MIL (c), and UiO/MIL/CN (d); TEM images of NH_2-MIL-125 (e), UiO-66 (f), UiO-on-MIL (g), and UiO/MIL/CN (h); and SEM-mapping of UiO/MIL/CN heterostructure (i-n).

2.2. Instrumentation

The morphology and microstructure of the different stages of synthesized catalysts were characterized using a FESEM technique TESCAN MIRA-II (Czechia) and TEM technique CM120 (Netherlands). The FT-IR technique model device PerkinElmer Spectrum Version 10.02.00 was used to identify the functional groups and their changes in different stages of the synthesized catalyst. The X-ray powder diffraction (XRD) patterns of the different stages of synthesized catalyst were detected by the X-ray diffractometer PHILIPS PW 3710. The N_2 adsorption-desorption technique with model device BELSORP-mini-II was used to determine the surface area and pore size of different stages of the synthesized catalyst. X-ray photoelectron spectroscopy (XPS) of the samples was shown on applied electron spectrometers Bes Tec (Germany). UV–visible reflectance spectra were obtained using a spectrophotometer UV-2550 (Japan), and bandgap values were determined Tauc Plot technique.

2.3. Fabrication of g-C_3N_4 nanosheets

The nanosheets g-C_3N_4 were fabricated through a thermal polymerization of melamine according to our previous findings [54,55] (details synthesis described in Text S1, Supporting Information).

2.4. Fabrication of UiO@MIL

UiO-66-on-NH_2-MIL-125 was fabricated using an epitaxial growth method under solvothermal conditions. Firstly, the as-prepared NH_2-MIL-125 (0.1 g, details synthesis provided in Text S2, Supporting Information) and PVP (0.1 g) as structure-director agents were dispersed into 10.0 mL DMF under sonication to form the uniform suspension. Subsequently, 0.105 g $ZrCl_4$ with 0.075 g H_2BDC was dispersed into DMF (42.0 mL)/HOAc (8.0 mL) to obtain a homogeneous solution. After that, the NH_2-MIL-125 suspension and $ZrCl_4$ with H_2BDC solution were mixed at room temperature for 30 min. Then, the mixture was transferred to a Teflon-lined autoclave and heated for 24 h at 120 °C to crystals UiO-66 growth onto NH_2-MIL-125. After completion of the reaction, the yellow product was washed several times with DMF and MeOH for purification.

2.5. Fabrication of UiO/MIL/CN

In terms of UiO/MIL/CN preparation, Firstly, 0.01 g of the g-C_3N_4 nanosheet was dispersed into 10 mL of MeOH under sonication. Subsequently, the as-obtained MOF-on-MOF crystals (0.20 g) were added to the balloon and subjected to reflux at 65 °C. After 2 h reaction, the resulting precipitate was cooled and centrifuged. For purification, the final composite was washed several times with methanol and dried at 80 °C under vacuum.

2.6. Photocatalytic degradation

The photocatalytic performance of UiO/MIL/CN for OFL degradation was assessed under visible light irradiation by a 300 W xenon lamp (OSRAM XBO, Germany with a light intensity of 2650 µm/cm^2) with a 420 nm filter (details experiment were described in Test S3, Support Information). The as-prepared photocatalysts were added at a concentration of 0.1 g L^{-1} to 50 mL solution containing the OFL (20 mg L^{-1}), then the suspension solution was stirred in the dark for 30 min before visible light irradiation. After this period, the lamp ($\lambda > 420$ nm) was shone and the decrease in the concentration of OFL in the solution. At regular time intervals, 3.0 mL of suspension was withdrawn and separated using a 0.22 µm mixed cellulose ester (MCE) membrane filter to remove any photocatalyst in the solution. Finally, the concentration of OFL was analyzed using the UV–Vis spectrophotometer (DR-6000) and LC-mass with Waters Alliance 2695 HPLC-Micromass Quattro micro API Mass Spectrometer (detailed experiment provided in Test S4, Support Information).

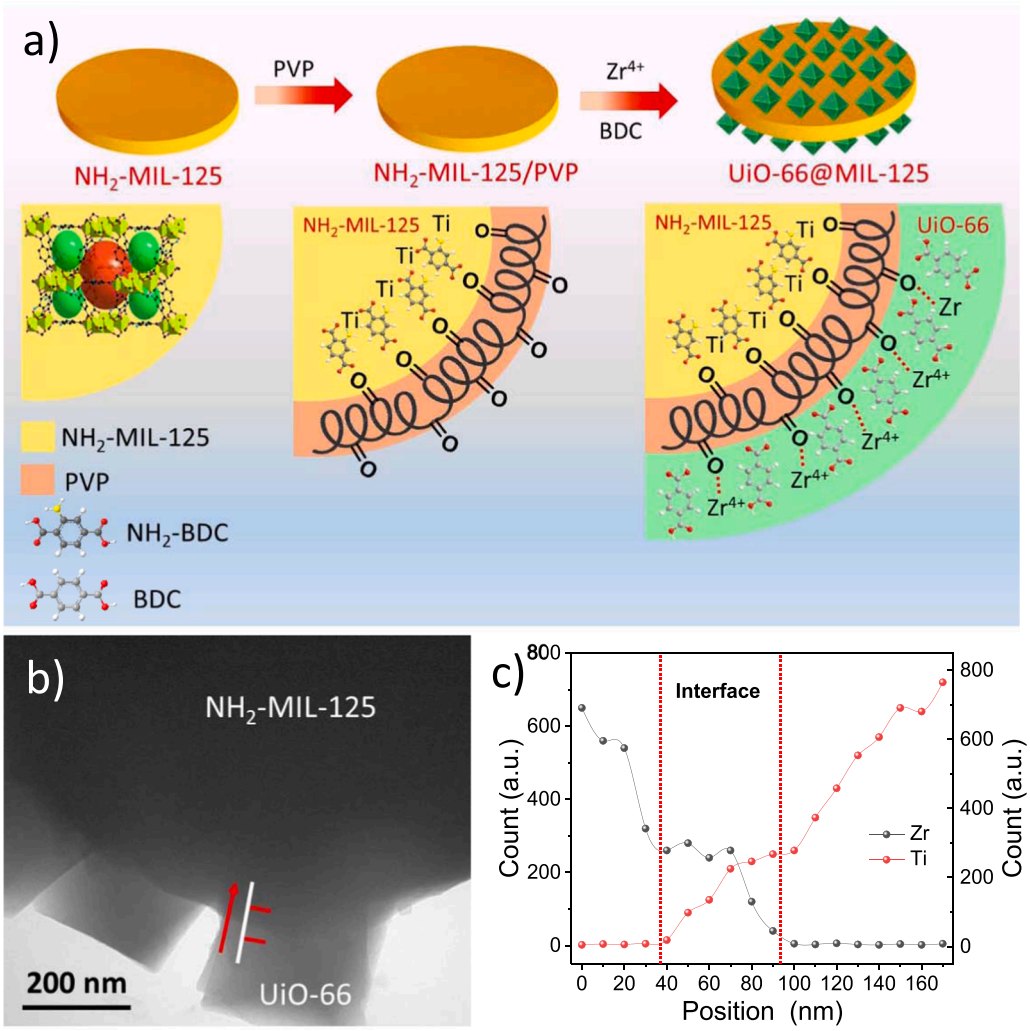


Fig. 3. (a) Schematic representation for the systematic growth of MOF-on-MOF heterostructure; TEM image (b) and corresponding EDX analysis data of the overlap junction of the MOF-on-MOF heterostructure (c).

2.7. Photocatalyst synthesis strategy

Fig. 1 describes the synthesis strategy of double Z-scheme UiO/MIL/CN heterojunction that comprised three steps: firstly, fabrication of tablet-like NH_2-MIL-125 as the host MOF secondly, epitaxial growth of UiO-66 crystals on the NH_2-MIL-125 surface via the solvothermal method, and finally decorating g-C_3N_4 nanosheets onto UiO-66@NH_2-MIL-125 surface for design new type of double Z-scheme heterojunction photocatalyst. Significantly, the conjugation of UiO-66 and NH_2-MIL-125 microporous alters some of the intrinsic properties of individual MOFs (including sensitivity to humidity, acidic, and thermal conditions) [19,37] and increases resistance to ROS in AOP. On the other hand, it enhances the photodegradation efficiency and makes separation easier.

3. Findings and discussion

3.1. Morphological analysis

Aiming to examine the epitaxial growth behavior of MOF-on-MOF, FESEM, and TEM techniques were evaluated. As depicted in Fig. 2a and e, pure NH_2-MIL-125 revealed a tablet-like morphology with a particle size of approximately 750 nm with a thickness of about 150 nm. In contrast, UiO-66 crystals displayed an octahedral morphology with a particle size of about 250 nm. After the epitaxial growth of the UiO-66 onto a tablet-like NH_2-MIL-125 surface, the size, structures, and morphology of both MOFs were preserved. Also, the FESEM (Fig. 2c) and TEM (Fig. 2g) images further indicated that the growth of UiO-66 microcrystals onto NH_2-MIL-125 surface was heterogeneous, which grew both at the surface and edges. This epitaxial growth of UiO-66 was formed due to the coordination phenomenon caused by PVP. By decorating g-C_3N_4 sheets on MOF-on-MOF surface, the structures and morphology of both MOF were preserved, but the crystals size of NH_2-MIL-125 became smaller (range 200–250 nm) and UiO-66 crystals larger (range 230–300 nm). This phenomenon was converted from the final nanostructure to composite heterojunction, confirmed by FESEM (Fig. 2d) and TEM images (Fig. 2h). Meanwhile, the use of the solvothermal method instead of reflux created a MOF-on-MOF structure with a rough surface, confirmed by FESEM and TEM images (Fig. S1, ESI). Also, SEM–mapping in Fig. 2i-n and EDS in Fig. S2, ESI has presented the purity and elements corresponding to UiO/MIL/CN hybrid structure.

3.2. Formation mechanism of MOF-on-MOF

How the two MOFs with different physicochemical structures make the heterostructured connection is a very challenging issue for nanomaterial architecture. This phenomenon may be due to the interaction between the polar groups of PVP and Zr^{4+} ions in UiO-66, which improves the affinity of UiO-66 to NH_2-MIL-125. According to the findings of Kitagawa and co-workers [37], the zeta potential of PVP was revealed

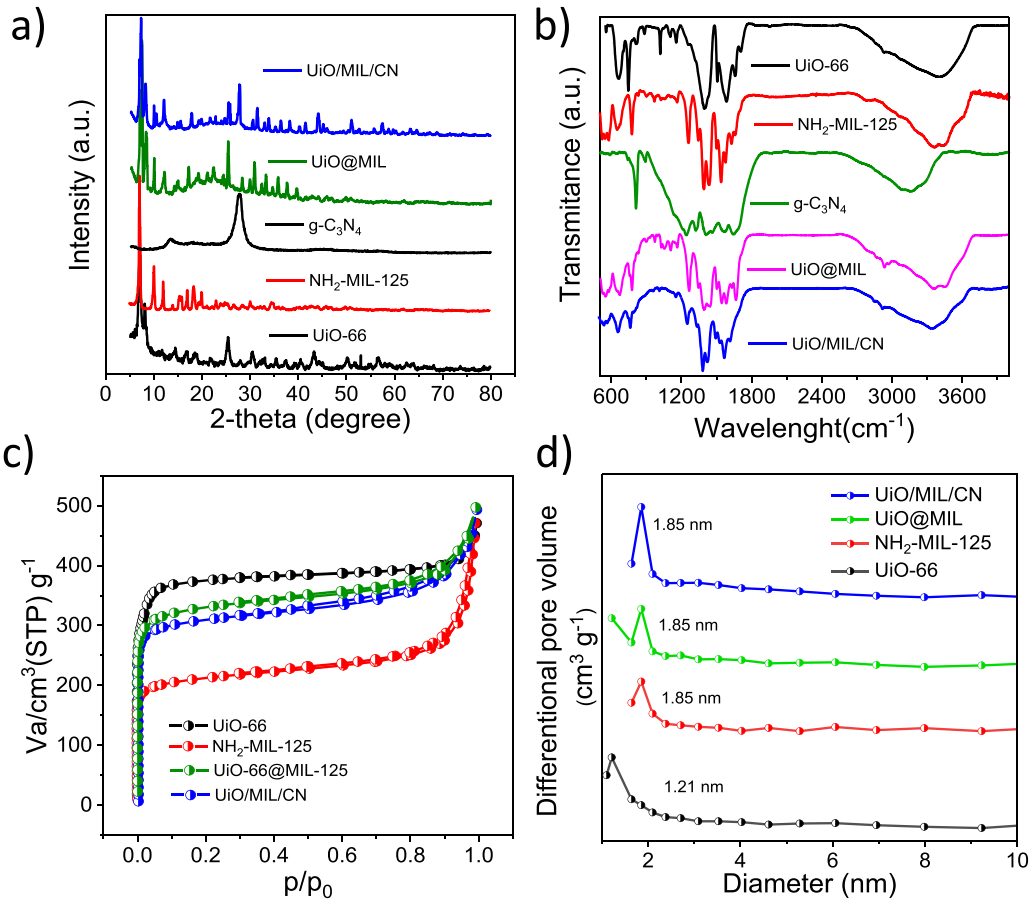


Fig. 4. HA-XRD pattern (a), FT-IR spectrum(b), N_2 adsorption-desorption isotherms (d), BJH plot of obtained photocatalysts.

a negative value (−0.27 mV), while UiO-66 is a positive value (+44.0 mV, Fig. S3, ESI), confirming the high affinity of UiO-66 to PVP/NH_2-MIL-125. As a result, the nuclei of UiO-66 were aggregated with NH_2-MIL-125 crystals to form micelles, and then an internal growth process occurred under solvothermal conditions (Fig. 3a). Meanwhile, epitaxial growth of UiO-66 on the edge of NH_2-MIL-125 might be due to the lattice match of $\{110\}_{NH2\text{-}MIL\text{-}125}/\{001\}_{UiO\text{-}66}$, which is further indicated by the TEM image (Fig. 3b) and EDX spectrum data (Fig. 3c).

3.3. Structures and compositions

The crystal and phase structures of obtained photocatalysts were analyzed using the HA–XRD pattern (Fig. 4a). The XRD pattern of pristine UiO-66 and NH_2-MIL-125 was consistent with the previous report [56,57]. Also, the typical peaks at $2\theta = 13.15°$ and 27.54° can be indexed to the crystal planes in g-C_3N_4 (JCPDS card No. 87–1526) [58]. The XRD pattern of MOF-on-MOF contained the characteristic peaks of both the UiO-66 and NH_2-MIL-125, confirming the successful combination of these two MOFs. Furthermore, the diffraction peaks of UiO/-MIL/CN heterostructure contain all the characteristic peaks of UiO-66 @NH_2-MIL-125 and g-C_3N_4, indicating the excellent decoration of g-C_3N_4 sheets on MOF-on-MOF.

FT-IR technique was used to analyze the chemical groups of photocatalysts. As depicted in Fig. 4b, the functional chemical groups of pristine UiO-66 and NH_2-MIL-125 were consistent with the previous report [59,60]. For pristine g-C_3N_4, the peaks at 815 and 1180–1720 cm^{-1} can be ascribed to the vibration of C═N and C-N tri-s-triazine units, respectively [61]. In the case of MOF-on-MOF, the broad peaks around 450–800 cm^{-1} were linked to the Ti-oxo clusters in NH_2-MIL-125 [56], as well as peak detected at 3571 cm^{-1} attributed to free μ_3-bridging hydroxyls belonging to Zr_6 clusters in UiO-66 [59]. In addition, peaks in the range of 1380–1640 indicate carboxyl stretching vibrations in both MOFs [59,60]. All the characteristic peaks of MOF-on-MOF and g-C_3N_4 appeared in UiO/MIL/CN heterostructure.

Nitrogen adsorption-desorption isotherms and the pore size distribution curve were evaluated to detect the porous nature of obtained photocatalysts. As depicted in Fig. 4c, UiO-66 indicated a typical type I isotherm with surface area $S_{BET} = 1520\ m^2\ g^{-1}$ and total pore $= 0.703\ cm^3\ g^{-1}$, while NH_2-MIL-125 revealed $S_{BET} = 813\ m^2\ g^{-1}$ and total pore $= 0.723\ cm^3\ g^{-1}$. Moreover, the S_{BET} of UiO-on-MIL was $637\ m^2\ g^{-1}$ and total pore $= 0.381\ cm^3\ g^{-1}$, demonstrating porous frameworks of both MOFs. After decorating g-C_3N_4 on the MOF-on-MOF surface, the S_{BET} and total pore of UiO/MIL/CN heterostructure were reduced to $774\ m^2\ g^{-1}$ and $0.480\ cm^3\ g^{-1}$, respectively. Using the technique of BJH (Fig. 4d), the corresponding pores diameter distributions of the MOF-on-MOF and UiO/MIL/CN were specified at 1.85 nm, confirming the microporous structure.

The chemical states and element composition of UiO/MIL/CN heterostructure were evaluated by XPS spectrum (Fig. 5). The survey spectrum of UiO/MIL/CN revealed the co-existence of carbon, nitrogen, oxygen, zirconium, and titanium, with atomic ratios of 51.3%, 18.3%, 29.1%, 0.5%, and 0.8%, respectively (Fig. 5a), which is in agreement with EDX results (Fig. S2, ESI). As displayed in Fig. 5b, the Ti 2p XPS spectrum of UiO/MIL/CN heterostructure contains peaks binding energies related to the 464.35 and 470.09 eV, demonstrating the presence of Ti $2p_{3/2}$ and Ti $2p_{1/2}$, respectively. Moreover, Zr 3d contains peaks binding energies 188.33 and 190.70 eV revealing Zr $3d_{5/2}$ and Zr $3d_{3/2}$, respectively (Fig. 5c). The presence of the Ti 2p and Zr 3d region in UiO/MIL/CN heterostructure confirmed the successful fabrication of MOF-on-MOF. Furthermore, the high-resolution XPS spectrum for C 1 s indicated four peaks located at 281.85, 286.97, 290.58, and 293.61 eV, which respectively correspond to the C═O, C-O, C-C, and N═C-O

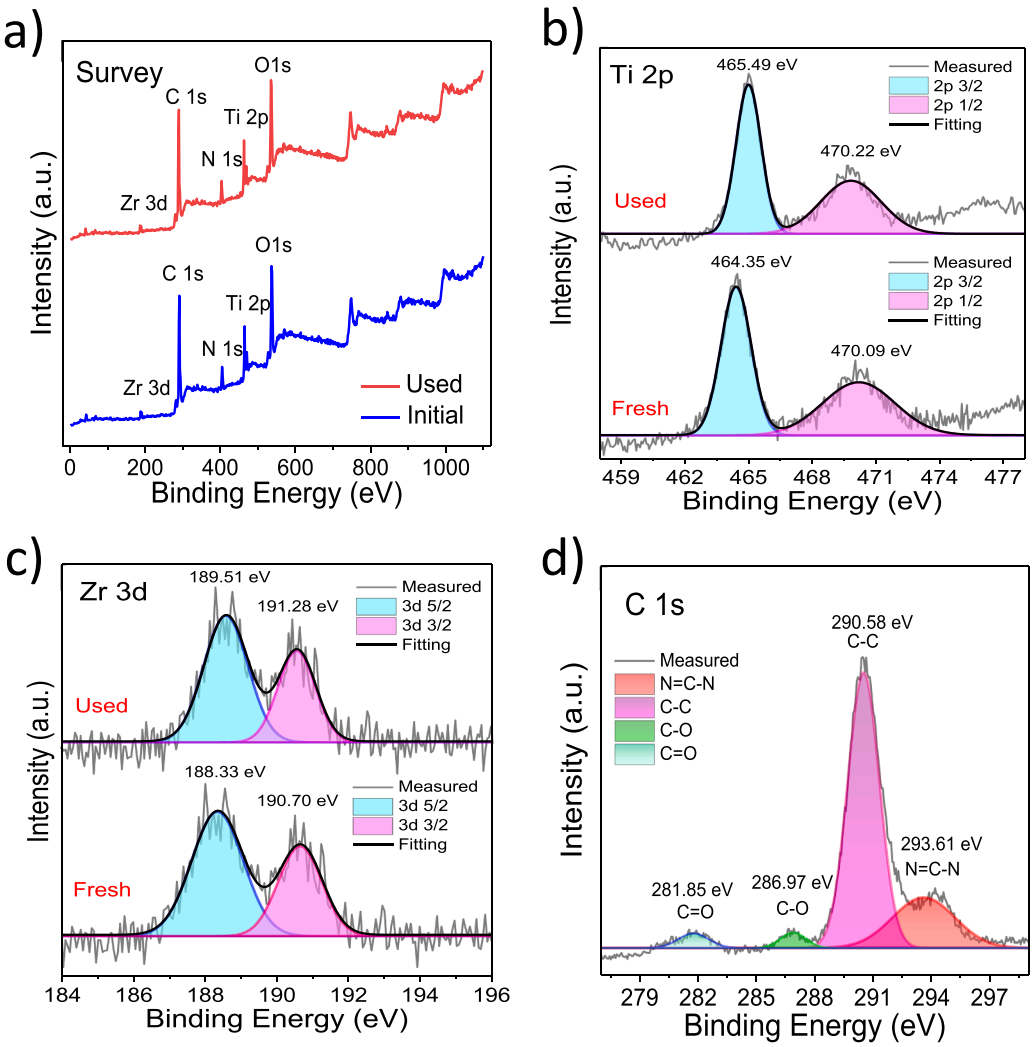


Fig. 5. XPS spectrum of the UiO/MIL/CN heterostructure: (a) survey spectrum, (b) Ti 2p, (c) Zr 3d, and (d) C 1s.

species (Fig. 5d). The appearance of the peak in the range of 293.6 eV proved that the g-C_3N_4 connected on MOF-on-MOF.

3.4. Photochemical properties

The optical response characteristics of as-obtained samples were investigated by UV–vis DRS spectra, and the results are shown in Fig. 6a. Similar to other reports, pristine UiO-66, NH_2-MIL-125, and g-C_3N_4 displayed an absorption edge at around 325, 445, and 460 nm, respectively. When UiO-66 crystals were grown onto the NH_2-MIL-125 surface, the absorption edge of the MOF-on-MOF shifted to a longer wavelength direction in comparison to individual MOFs. After combining g-C_3N_4 and MOF-on-MOF, the light absorption capacity UiO/MIL/CN heterojunction for visible light was enhanced, which could promote the photocatalytic activity in AOP. Based on these absorption edges and the Tauc plot method (Text S5 in Support Information), the bandgap energies of UiO-66, NH_2-MIL-125, and g-C_3N_4 were estimated as 3.82, 2.86, and 2.68 eV, respectively, which were very near to the previous reports [62–65]. According to Mott-Schottky plot (Fig. 6c-e), the flat-band (E_{fb}) potentials g-C_3N_4, NH_2-MIL-125, and UiO-66 were estimated to be − 1.28, + 0.12, and − 0.81 eV vs. Ag/AgCl, which can be converted to − 1.08, − 0.31, and − 0.6 eV vs. NHE, respectively. Combining these values with the E_g ones evaluated by the Tauc plots (Fig. 6b), the valence band potentials (E_{VB}) of g-C_3N_4, NH_2-MIL-125, and UiO-66 were estimated to be + 1.60, + 3.17, and + 3.22 eV vs. NHE by using the equation ($E_{VB} = E_{CB} + E_g$) [13]. As shown in Fig. 6f, the bands of the three photocatalysts revealed a cross arrangement, describing the characteristic charge transfer route of a double Z-scheme heterojunction.

3.5. Photocatalytic activity

3.5.1. Photodegradation of OFL in different systems

Photochemical AOPs were generally recognized as being an efficient strategy for removing pollutants. Therefore, the potential use of double Z-scheme UiO/MIL/CN heterojunction as an efficient photocatalyst was explored for OFL degradation. Initially, to evaluate the photocatalytic performance of UiO/MIL/CN, the removal of OFL was carried out in the darkness to reach adsorption-desorption equilibrium. Using UiO/MIL/CN in darkness resulted in the adsorption of 18.4% of OFL, while the UiO-66 has the highest adsorption (22.8%) capacity of OFL compared to other prepared photocatalysts, demonstrating a high specific surface area (1520 $m^2 g^{-1}$, Fig. 4c). Under visible light irradiation, UiO/MIL/CN heterojunction degraded more than 99.1% OFL during 50 min (Fig. 7a, b), which can compete with the best photocatalyst systems (Table S1, ESI). Meanwhile, the degradation of OFL under visible light followed the order of UiO/MIL/CN > UiO@MIL > MIL/CN > NH_2-MIL-125 > UiO/CN > g-C_3N_4 > UiO-66 after 50 min

Moreover, the photodegradation tests followed the pseudo-first-order-kinetic model (Eq. (1)). The rate constant (k) of UiO/MIL/CN

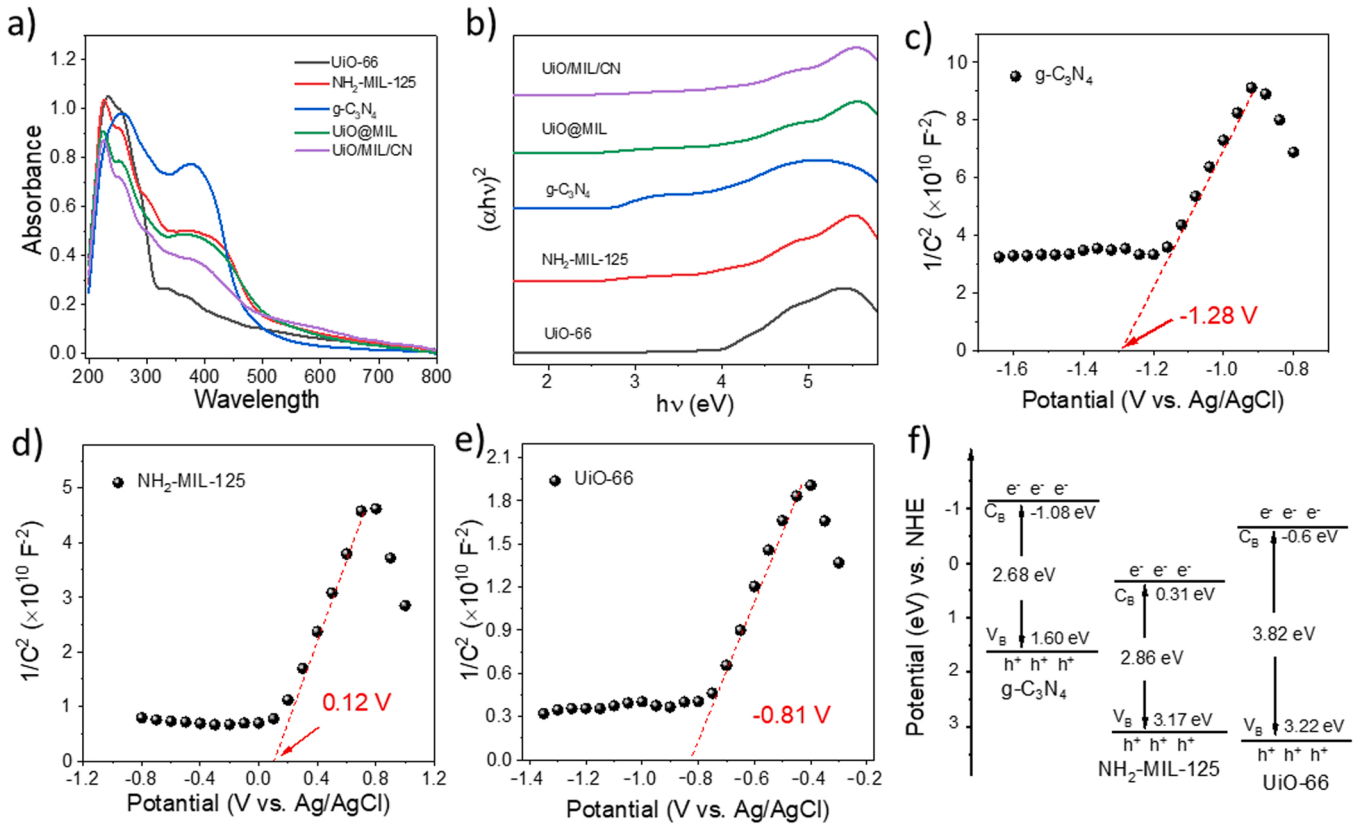


Fig. 6. UV–vis DRS spectrum (a), Tauc plots of prepared photocatalysts (b), Mott−Schottky plots of g-C_3N_4 (c), NH_2-MIL-125 (d), UiO-66 (e), and bandgap structures of g-C_3N_4, NH_2-MIL-125, UiO-66 (f).

heterostructure was almost 1.79 times higher than that of UiO@MIL (Fig. 7c), illuminating that the high concentration of ROS generated and further confirmed by the results of EPR spectra (Fig. 8c-e). In order to eliminate the influence of specific surfaces, normalized reaction rate constant ($k_{normalized}$) indicated that the proposed heterostructure was about 1.47 times higher than that of UiO@MIL (Table S2, ESI).

$$-\ln(C_{[OFL]t} / C_{[OFL]0}) = k\ t \quad (1)$$

The findings indicated that ultrasonic waves [66] and additive peroxymonosulfate (PMS) [67] could quickly produce ROS to degrade contaminants. Therefore, degradation of OFL was conducted without visible light irradiation under sonication (40 Hz/250 W) and 0.2 g L^{-1} PMS (less than the sulfate ion concentration suggested by the U.S. EPA [68]) in the presence of 0.1 g L^{-1} UiO/MIL/CN. As depicted in Fig. 7d, OFL in the absence of visible light irradiation did not show significant sono-degradation and PMS-assisted degradation, illustrating that ROS generation in these systems is unfavorable.

OFL wastewater samples utilizing deionized water, tap water, river water, and wastewater were chosen to evaluate the global applicability of the photocatalytic system. It can be seen from Fig. 7e that a suitable photodegradation rate of up to 82% was obtained in both river and tap water, while wastewater indicated only 68.5%. These results might be attributed to the high inorganic anions concentration and the reaction with ROS generated in the photodegradation process.

Also, the reactions on a 10.0 L scale were applied to assess the scalability of as-obtained photocatalysts under visible light irradiation. As depicted in Fig. 7f, the double Z-scheme UiO/MIL/CN heterojunction displayed remarkable photocatalytic behavior on large scales. These findings reveal that the proposed protocol is operationally simple, sustainable, scalable, and works to photodegrade contamination in light conditions rapidly.

3.5.2. *Effects of dosage catalyst, pH, and OFL concentrations*

The dosage of photocatalysts can affect the adsorption and photodegradation behaviors of OFL antibiotics. As displayed in Fig. S4, ESI, the photodegradation of OFL after 50 min improved from 65% to 99.1% when the concentration of UiO/MIL/CN heterojunction was increased from 0.04 g L^{-1} to 0.1 g L^{-1}. This performance improvement can be attributed to the increase in the active sites of the photocatalyst, which leads to the production of large amounts of ROS. Moreover, by increasing the amount of photocatalyst to above 0.15 g L^{-1}, the turbidity of the suspension was increased, and the penetration of light into the suspension decreased, which caused a reduction in photodegradation performance.

The initial solution pH is a crucial factor that influences the photodegradation system. Therefore, the photodegradation of OFL by UiO/MIL/CN heterojunction was evaluated in the pH range of 3.0, 5.0, 7.0, 9.0, and 11.0. The results in Fig. S5, ESI indicated that in pH 5.0–9.0, proper photodegradation was observed, while in pH= 3.0 and 11.0, the removal rates of OFL were 66.9% and 59.2%, respectively. This decrease in photodegradation rates may be to the inhibitory influence of H^+ and OH^- ions on the generated free radicals.

Moreover, increasing the OFL concentration from 20 to 50 mg L^{-1} resulted in a decrease significantly in the photodegradation efficiency from 99.1% to 51.8% (Fig. S6, ESI). This phenomenon can be related to the reactive surfaces on the catalyst surface becoming saturated with OFL, and the light contact with the photocatalyst surface decreases, resulting in a decrease in ROS.

3.5.3. *Effects of inorganic anions*

The photodegradation behaviors of antibiotics can affect by the inorganic anions in wastewater. A series of experiments were evaluated to confirm the positive or negative influence of anions on OFL photodegradation. As depicted in Fig. 8a, the presence of Cl^-, NO_3^-, and SO_4^{2-}

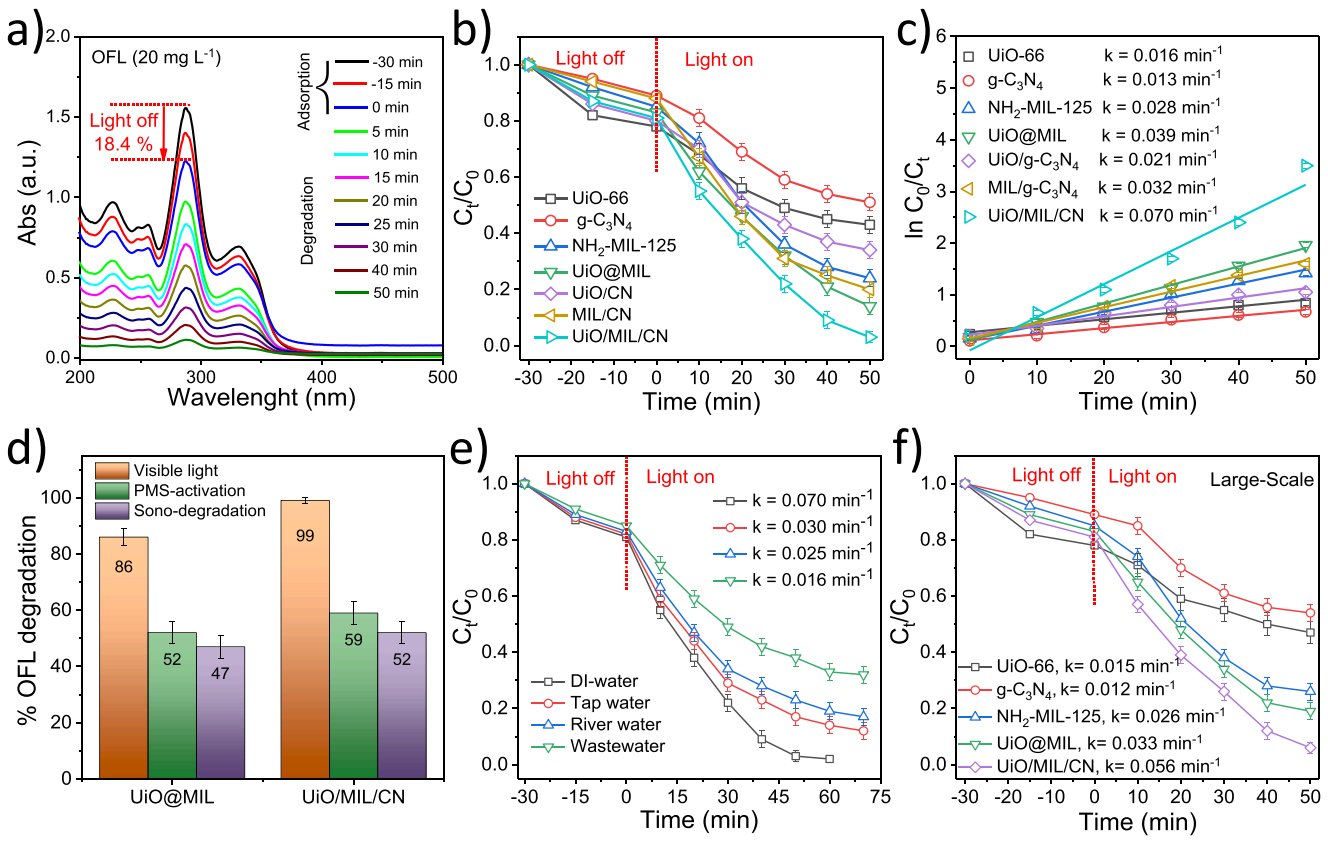


Fig. 7. Effect of some parameters on OFL photodegradation: (a) UV–vis spectrum; (b) various as-prepared photocatalysts; (c) kinetics of OFL photodegradation; (d) effect of different methods for OFL degradation.; (e) influence of various water quality conditions; and (f) OFL photodegradation in large-scale. Experimental conditions: [OFL] = 20 mg L^{-1}, [photocatalysts] = 100 mg L^{-1}, without adjustment pH.

slightly influenced OFL photodegradation. Furthermore, HCO_3^- and HPO_4^{2-} had a significant impact on photodegradation that might be due to scavenging $^{\bullet}OH$ and h^+ radicals to generate $CO_3^{\bullet-}$ and $PO_4^{\bullet 2-}$ radicals [69] Eqs. (2)–(5).

$$HCO_3^- + h^+ \rightarrow CO_3^{\bullet-} + H^+ \quad (2)$$

$$HCO_3^- + {}^{\bullet}OH \rightarrow CO_3^{\bullet-} + HOH \quad (3)$$

$$HPO_4^{2-} + h^+ \rightarrow PO_4^{\bullet 2-} + H^+ \quad (4)$$

$$HPO_4^{2-} + {}^{\bullet}OH \rightarrow PO_4^{\bullet 2-} + HOH \quad (5)$$

3.6. Photocatalytic mechanism

3.6.1. Identification of ROS

To further evaluate the contributions of ROS, the photocatalytic degradation of OFL photodegradation was conducted in the presence of various radical scavengers. The experiments were carried out using 10 mM of EDTA-2Na (h^+ scavenger), $K_2Cr_2O_7$ (e^- scavenger), BQ ($^{\bullet}O_2^-$ scavenger), and TBA ($^{\bullet}OH$ scavenger) under visible light irradiation [70]. The results in Fig. 8b exhibited that EDTA-2Na hardly affects the dynamics of OFL photodegradation, illustrating that h^+ was unlikely to be responsible for photodegradation. Meanwhile, TBA and BQ significantly inhibited the OFL photodegradation, reducing the removal of OFL to 42.5% and 23.8%, respectively. Additionally, the EPR technique (Fig. 8c-e) further confirmed that $HO^{\bullet}$ and $^{\bullet}O_2^-$ radicals participated in photodegradation, but $^{\bullet}O_2^-$ radicals might play a dominant role during the photocatalytic system of OFL degradation over double Z-scheme UiO/MIL/CN heterojunction. Also, a total organic carbon (TOC) removal efficiency of 45.2%, 54.3%, 58.7%, and 77.9% were evaluated after 50 min of photodegradation for UiO-66, g-C_3N_4, NH_2-MIL-125, and double Z-scheme UiO/MIL/CN heterojunction, respectively (Fig. 8f). The high value of TOC removal for the double Z-scheme UiO/MIL/CN heterojunction confirms the excellent mineralization of OFL under visible light irradiation.

3.6.2. Photocatalytic reaction mechanism

Based on the above results, a possible photocatalytic mechanism was proposed for OFL photodegradation and schematically described in Fig. 9. In the II-scheme, the photogenerated electrons are transferred from the CB of the g-C_3N_4 and CB of UiO-66 to the CB of the NH_2-MIL-125 through the II-scheme mechanism. Meanwhile, the holes in the VB of the UiO-66 migrate to the VB of the NH_2-MIL-125 and then to g-C_3N_4. Consequently, the electrons accumulate in the CB of the NH_2-MIL-125, and the holes gather in the VB of the g-C_3N_4. This charge transfer mechanism leads to a decreased redox ability of electrons and holes. The electrons in the CB of NH_2-MIL-125(Ti) cannot reduce O_2 into $^{\bullet}O_2^-$ radicals due to its CB potential being more positive than the $O_2/^{\bullet}O_2^-$ potential (−0.33 V vs. NHE) [70], which is not in agreement with the obtained EPR results (Fig. 8c-e). Moreover, the holes accumulated in the VB of g-C_3N_4 cannot oxidize H_2O to $^{\bullet}OH$ due to VB potential of g-C_3N_4 (1.60 eV) is more negative than the $H_2O/^{\bullet}OH$ potential (1.99 V vs. NHE) [70]. In this case, $^{\bullet}O_2^-$ and $^{\bullet}OH$ are not generated in the photocatalytic process, which is contrary to the EPR results (Fig. 8c-e). Therefore, the traditional type-II model was not reliable for the process of OFL photodegradation. The direct double Z-scheme mechanism is more reasonable for UiO/MIL/CN heterojunctions in comparison with the II-scheme mechanism. According to the double Z-scheme heterojunction mechanism, the photogenerated electrons formed on the CB of NH_2-MIL-125 recombine with the holes in the VB of g-C_3N_4 and UiO-66. The produced electrons in CB of NH_2-MIL-125 can migrate rapidly to the valence band

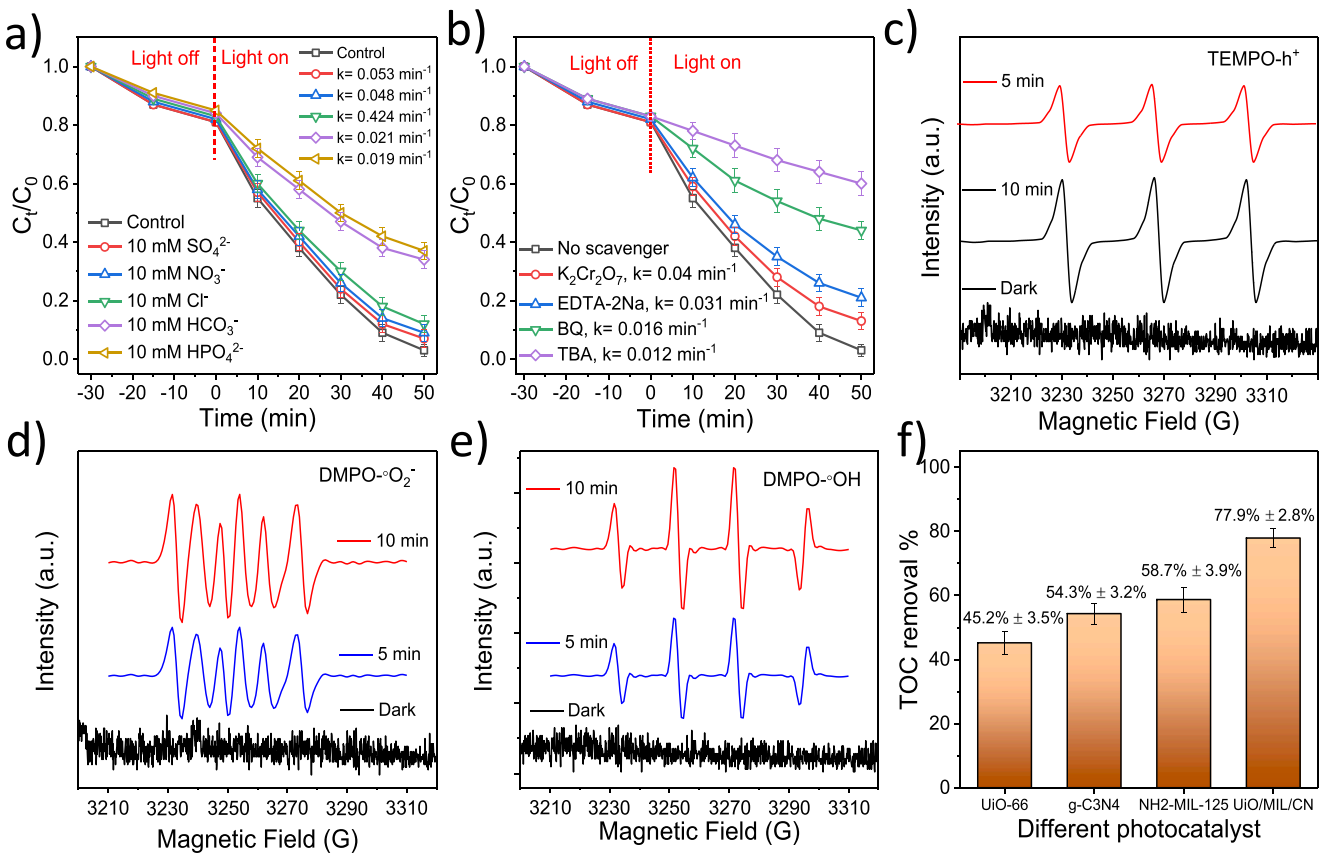


Fig. 8. (a) Effect of inorganic anions and (b) different quenchers on the OFL photocatalytic degradation by double Z-scheme UiO/MIL/CN heterojunction; EPR signals of (d) TEMPO-h^+, DMPO-$^{\bullet}O_2^-$, and (e) DMPO-$^{\bullet}OH$ of UiO/MIL/CN under dark and visible light irradiation; and (f) TOC analysis under various as-prepared photocatalysts. Reaction condition: [OFL] = 20 mg L^{-1}, [photocatalyst] = 100 mg L^{-1} [inorganic anions] = 10 mM, [quencher] = 10 mM, without adjustment pH.

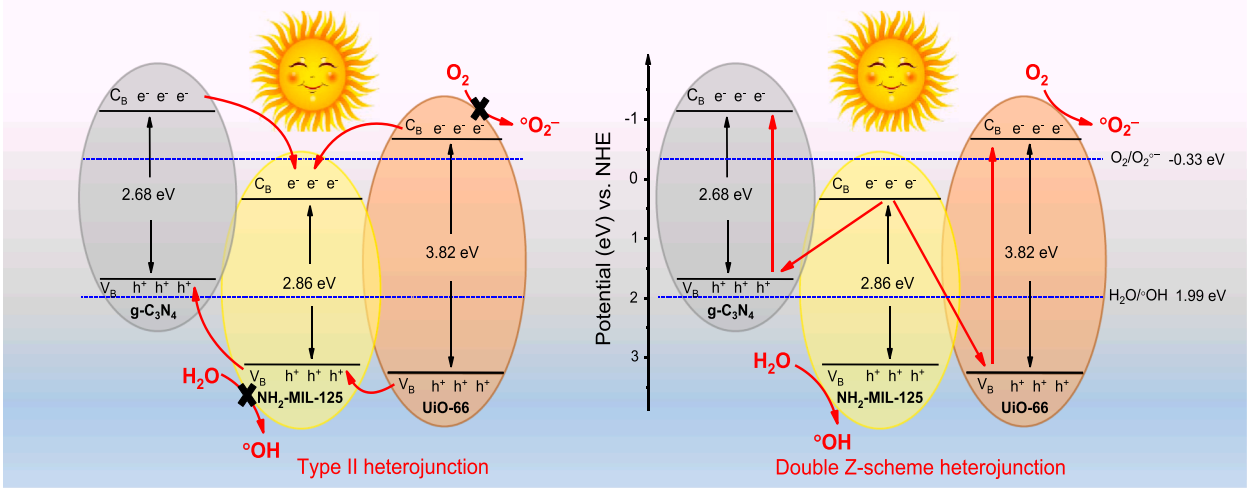


Fig. 9. Schematic representation of reaction mechanism of UiO/MIL/CN photocatalyst.

of g-C_3N_4 and UiO-66 and electrostatically recombine with the generated holes. Hence, the photogenerated electrons in the CB of the g-C_3N_4 (−1.08 V) and UiO-66 (−0.6 V) could reduce O_2 to $^{\bullet}O_2^-$ due to their CB potentials are more negative than the $O_2/^{\bullet}O_2^-$ potential (−0.33 V vs. NHE) [70]. Meanwhile, the photogenerated holes in the VB of the NH_2-MIL-125 and UiO-66 (3.17 and 3.22 V) can activate H_2O molecules to form $^{\bullet}OH$ due to the VB of both NH_2-MIL-125 and UiO-66 being positive than that of $H_2O/^{\bullet}OH$ (1.99 V vs. NHE) [70]. Eventually, these ROS ($^{\bullet}O_2^-$ and $^{\bullet}OH$ radicals) can efficiently degrade and mineralize OFL antibiotics. Therefore, the double Z-scheme mechanism in comparison with the II-scheme mechanism can suitable for UiO/MIL/CN heterojunctions. The OFL photodegradation equation may be as follows (Eqs. (6)–(9)).

$$\text{UiO/MIL/CN} + \text{visible light} \rightarrow e^- + h^+ \quad (6)$$

$$h^+ + H_2O + OH^- \rightarrow {}^{\bullet}OH \quad (7)$$

$$e^- + O_2 \rightarrow O_2^{\bullet-} \quad (8)$$

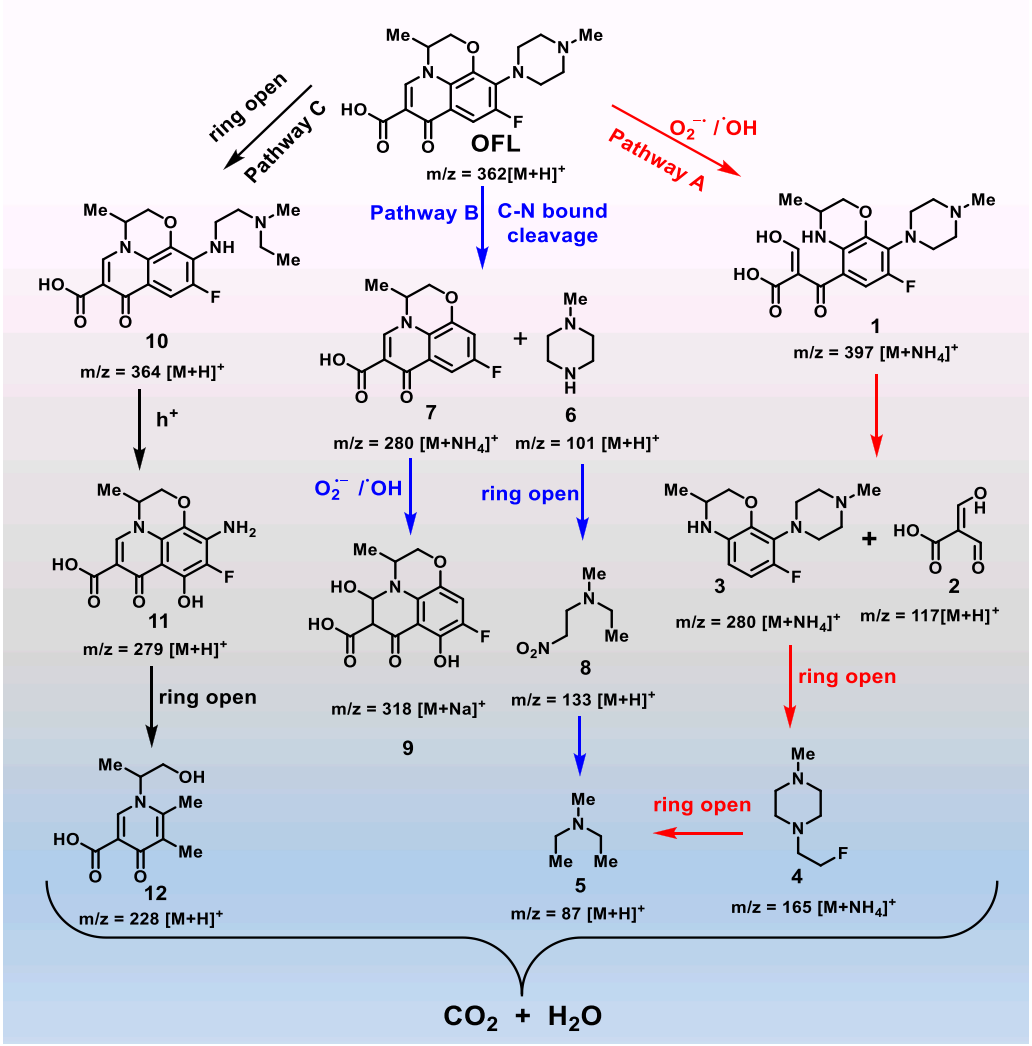


Fig. 10. Proposed photoexcited pathway of OFL by double Z-scheme UiO/MIL/CN heterojunction.

$$O_2^{\bullet -}/{}^{\bullet}OH/h^+ + OFL \rightarrow \text{intermediates} \rightarrow CO_2 + H_2O \quad (9)$$

3.6.3. Proposed pathways of OFL photodegradation

Scientific findings in recent years revealed that the degradation of OFL in photocatalytic systems leads to different intermediates. For example, Gong et al. [71] reported that the intermediate products of OFL degradation were formed through the demethylation and $^{\bullet}OH$ attacked route in UiO-66/wood system. Also, Liu et al. [72] reported four OFL degradation pathways including oxidation, dealkylation, hydroxylation, and cleavage of the piperazine ring route in g-C_3N_4/$NaNbO_3$ system. In the current study, three OFL photodegradation pathways were proposed according to LC-MS results as depicted in Fig S7, ESI. Pathways A are related to the cleavage piperazine ring, pathways B C-N bond cleavage between the piperazine ring and benzene, and pathways C hydroxylation on the tetrahydropyridine ring. Based on the photodegradation intermediates obtained in Fig. S7, and listed in Table S3, a possible degradation pathway was proposed. As shown in Fig. 10, in pathway A, intermediate 1 (*m/z* 397) was generated with hydroxylation on the tetrahydropyridine ring and ring cleavage after being attacked by $^{\bullet}O_2^-/{}^{\bullet}OH$ radicals. Besides, intermediate 2 (*m/z* 117) and intermediate 3 (*m/z* 282) were generated via break of the C-C bond between the carboxylic acid and benzene binding. Ultimately, intermediate 3 could convert to intermediate 4 (*m/z* 165), which might produce intermediate 5 (*m/z* 87). In pathway B, intermediate 6 (*m/z* 101) and intermediate 7 (*m/z* 280) were generated from the cleavage of the C-N bond of the piperazine ring and benzene binding. Thereafter, intermediate 8 (*m/z* 133) was generated by the break on the piperazine ring of intermediate 6 and subsequent could also produce into intermediate 5. Furthermore, intermediate 7 might be dehydroxylated to form intermediate 9 (*m/z* 318) due to the attack of $^{\bullet}O_2^-/{}^{\bullet}OH$ radicals. In pathway C, the broken piperazine ring might be attacked by h^+ to produce intermediate 10 (*m/z* 364), which could further generate intermediate 11 (*m/z* 279) via C-N bond cleavage. Finally, intermediate 12 (*m/z* 228) could be generated from the broken benzene binding by $^{\bullet}O_2^-/{}^{\bullet}OH$ radicals attack.

3.7. Reusability and stability

To evaluate the reusability of the double Z-scheme UiO/MIL/CN heterojunction, a reusing test was accomplished for four photocatalytic runs (Fig. 11a). After four cycles, the photocatalytic activity decreases marginally with 88.5% removal of the OFL, illustrating the great reusability of this photocatalytic system. As presented in Table S4, ESI, the concentrations of leached Ti and Zr in each test remain ~ 0.07 mg L^{-1}, which is extremely low and did not change significantly during different cycles. Furthermore, the XPS plot (Fig. 4c, d), XRD pattern (Fig. 11b), FESEM, and TEM images (Fig. 11c, d) of the photocatalyst recovered after four runs indicated that double Z-scheme UiO/MIL/CN

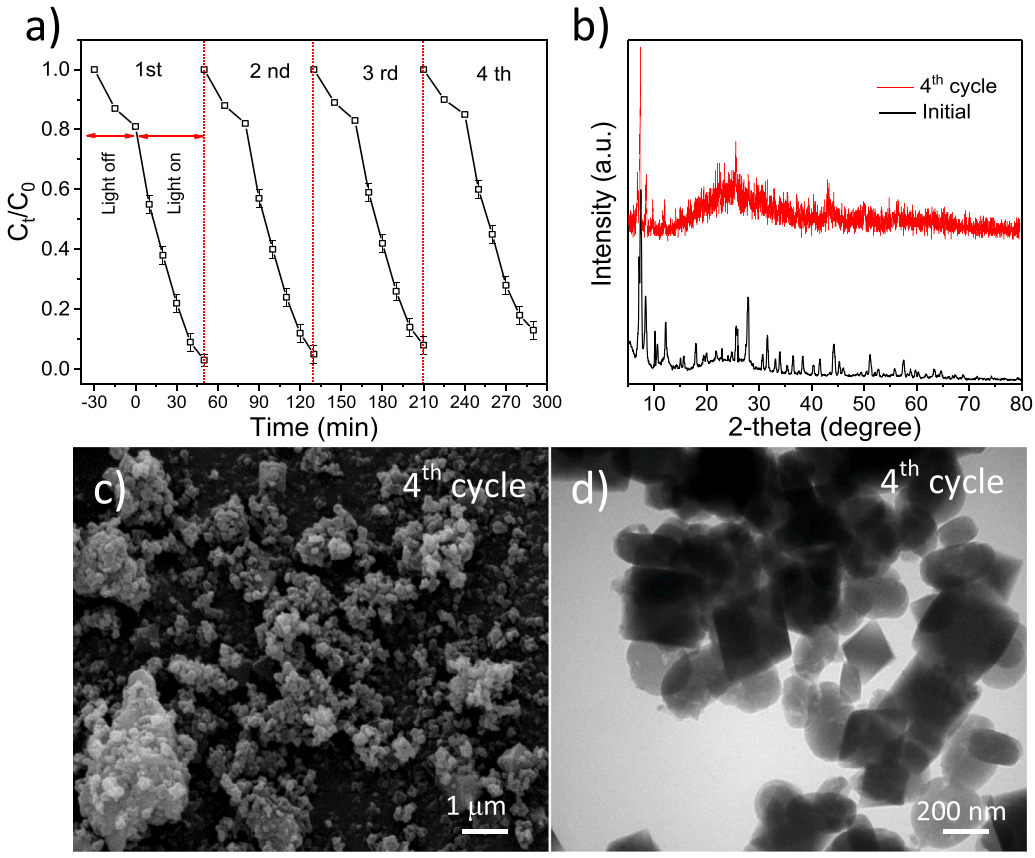


Fig. 11. (a) Reusability experiments of photodegrading OFL over UiO/MIL/CN heterojunction; (b) XRD pattern; (c,d) FESEM and TEM images of UiO/MIL/CN after four-cycle reaction: [OFL] = 20 mg L^{-1}, photocatalyst = 100 mg L^{-1}, without adjustment pH.

heterojunction remains intact, which confirms the remarkable stability of the photocatalyst and highlighting its resistance to ROS.

4. Conclusion

In this study, a new generation of double Z-scheme UiO/MIL/CN heterojunction was designed firstly and successfully fabricated for OFL photodegradation. The findings obtained from the spectroscopies analysis confirmed epitaxial growth of UiO-66 crystals onto the NH_2-MIL-125 as well as the decoration of g-C_3N_4 sheets onto the MOF-on-MOF surface. The proposed double Z-scheme heterojunction revealed dramatic enhancement in photocatalytic activity towards OFL degradation under visible light. Moreover, investigation of the reaction mechanism, quenching tests, and EPR technique also confirmed that $^{\bullet}OH$ and $^{\bullet}O_2^-$ radicals play a significant role in OFL photodegradation. Ulteriorly, the current study furnishes the finest route for the architecture MOF on other MOFs and also the fabrication of the double Z-scheme heterojunction materials for improvement in water treatment and clean energy production.

CRediT authorship contribution statement

Hassan Sepehrmansourie: Investigation in fabrication nanomaterials. **Hassan Alamgholiloo:** Supervision, Methodology, Writing - original draft, Investigation in photodegradation, Write the manuscript. **Nader Noroozi Pesyan:** Writing – review & editing. **Mohammad Ali Zolfigol:** Supervision, Writing – review & editing, Funding acquisition.

Declaration of Competing Interest

The authors declare that they have no known competing financial interests or personal relationships that could have appeared to influence the work reported in this paper.

Data availability

No data was used for the research described in the article. The datasets used and/or analyzed during the current study available from the corresponding author on reasonable request.

Acknowledgments

We gratefully acknowledge financial support from Bu-Ali Sina University and Iran National Science Foundation (INSF) (Grant Number: 4004528) for financial support. Furthermore, the authors thanks for the support from the laboratory of the Faculty of Chemistry, Urmia University.

Appendix A. Supplementary material

Supplementary data associated with this article can be found in the online version at doi:10.1016/j.apcatb.2022.122082.

References

[1] M. Patel, R. Kumar, K. Kishor, T. Mlsna, C.U. Pittman Jr, D. Mohan, Pharmaceuticals of emerging concern in aquatic systems: chemistry, occurrence, effects, and removal methods, Chem. Rev. 119 (2019) 3510–3673.
[2] Y. Hu, C. Zhou, H. Wang, M. Chen, G. Zeng, Z. Liu, Y. Liu, W. Wang, T. Wu, B. Shao, Recent advance of graphene/semiconductor composite nanocatalysts: synthesis, mechanism, applications and perspectives, Chem. Eng. J. 414 (2021), 128795.
[3] W. Yang, M. Zhou, N. Oturan, M. Bechelany, M. Cretin, M.A. Oturan, Highly efficient and stable $Fe^{II}Fe^{III}$ LDH carbon felt cathode for removal of pharmaceutical ofloxacin at neutral pH, J. Hazard. Mater. 393 (2020), 122513.

[4] E.M. Rodriguez, G. Marquez, M. Tena, P.M. Álvarez, F.J. Beltran, Determination of main species involved in the first steps of TiO_2 photocatalytic degradation of organics with the use of scavengers: the case of ofloxacin, Appl. Catal. B 178 (2015) 44–53.

[5] K. Kümmerer, Antibiotics in the aquatic environment-a review-part I, Chemosphere 75 (2009) 417–434.

[6] L. Jing, Y. Xu, J. Liu, M. Zhou, H. Xu, M. Xie, H. Li, J. Xie, Direct Z-scheme red carbon nitride/rod-like lanthanum vanadate composites with enhanced photodegradation of antibiotic contaminants, Appl. Catal. B 277 (2020), 119245.

[7] R. Xie, X. Meng, P. Sun, J. Niu, W. Jiang, L. Bottomley, D. Li, Y. Chen, J. Crittenden, Electrochemical oxidation of ofloxacin using a TiO_2-based SnO_2-Sb/polytetrafluoroethylene resin-PbO_2 electrode: reaction kinetics and mass transfer impact, Appl. Catal. B 203 (2017) 515–525.

[8] I.A. Ricardo, E.A. Alberto, A.H.S. Júnior, D.L.P. Macuvele, N. Padoin, C. Soares, H. G. Riella, M.C.V. Starling, A.G. Trovó, A critical review on microplastics, interaction with organic and inorganic pollutants, impacts and effectiveness of advanced oxidation processes applied for their removal from aqueous matrices, Chem. Eng. J. 424 (2021), 130282.

[9] M. Coha, G. Farinelli, A. Tiraferri, M. Minella, D. Vione, Advanced oxidation processes in the removal of organic substances from produced water: Potential, configurations, and research needs, Chem. Eng. J. 414 (2021), 128668.

[10] C. M. M′arimi, A.K. Mecha, R. Kiprop Ramkat, Recent trends in applications of advanced oxidation processes (AOPs) in bioenergy production, Renew. Sustain. Energy Rev. 121 (2020), 109669.

[11] Y. Shang, X. Xu, B. Gao, S. Wang, X. Duan, Single-atom catalysis in advanced oxidation processes for environmental remediation, Chem. Soc. Rev. 50 (2021) 5281–5322.

[12] S. He, C. Zhai, M. Fujitsuka, S. Kim, M. Zhu, R. Yin, L. Zeng, T. Majima, Femtosecond time-resolved diffuse reflectance study on facet engineered charge-carrier dynamics in Ag_3PO_4 for antibiotics photodegradation, Appl. Catal. B 281 (2021), 119479.

[13] X. Yang, Z. Chen, W. Zhao, C. Liu, X. Qian, M. Zhang, G. Wei, E. Khan, Y.H. Ng, Y. S. Ok, Recent advances in photodegradation of antibiotic residues in water, Chem. Eng. J. 405 (2021), 126806.

[14] M.M. Mahlambi, C.J. Ngila, B.B. Mamba, Recent developments in environmental photocatalytic degradation of organic pollutants: the case of titanium dioxide nanoparticles-a review, J. Nanomater. 2015 (2015) 5.

[15] D. Spasiano, R. Marotta, S. Malato, P. Fernandez-Ibanez, I. Di Somma, Solar photocatalysis: Materials, reactors, some commercial, and pre-industrialized applications. A comprehensive approach, Appl. Catal. B 170 (2015) 90–123.

[16] T. Li, J.E. Sullivan, N.L. Rosi, Design and preparation of a core-shell metal-organic framework for selective CO_2 capture, J. Am. Chem. Soc. 135 (2013) 9984–9987.

[17] P. Falcaro, A.J. Hill, K.M. Nairn, J. Jasieniak, J.I. Mardel, T.J. Bastow, S.C. Mayo, M. Gimona, D. Gomez, H.J. Whitfield, A new method to position and functionalize metal-organic framework crystals, Nat. Commun. 2 (2011) 1–8.

[18] K.-Y. Wang, L. Feng, T.-H. Yan, J.-S. Qin, C.-X. Li, H.-C. Zhou, Morphology transcription in hierarchical MOF-on-MOF architectures, ACS Mater. Lett. 3 (2021) 738–743.

[19] M.-X. Wu, Y. Wang, G. Zhou, X. Liu, Core-shell MOFs@MOFs: diverse designability and enhanced selectivity, ACS Appl. Mater. Interfaces 12 (2020) 54285–54305.

[20] Y. Wang, H. Li, X. He, Z. Xu, Application in anticounterfeiting for multistimuli smart luminescent materials based on MOF-on-MOF, Inorg. Chem. 60 (2021) 15001–15009.

[21] Q. Zha, F. Yuan, G. Qin, Y. Ni, Cobalt-based MOF-on-MOF two-dimensional heterojunction nanostructures for enhanced oxygen evolution reaction electrocatalytic activity, Inorg. Chem. 59 (2020) 1295–1305.

[22] K. Zhu, R. Fan, J. Wu, B. Wang, H. Lu, X. Zheng, T. Sun, S. Gai, X. Zhou, Y. Yang, MOF-on-MOF membrane with cascading functionality for capturing dichromate ions and p-arsanilic acid turn-on sensing, ACS Appl. Mater. Interfaces 12 (2020) 58239–58251.

[23] Y. Mei, Y. Cong, S. Huang, J. Qian, J. Ye, T.-T. Li, MOF-on-MOF strategy to construct a nitrogen-doped carbon-incorporated CoP@Fe-CoP core-shelled heterostructure for high-performance overall water splitting, Inorg. Chem. 61 (2021) 1159–1168.

[24] S. Kampouri, F.M. Ebrahim, M. Fumanal, M. Nord, P.A. Schouwink, R. Elzein, R. Addou, G.S. Herman, B. Smit, C.P. Ireland, Enhanced visible-light-driven hydrogen production through MOF/MOF heterojunctions, ACS Appl. Mater. Interfaces 13 (2021) 14239–14247.

[25] J. Yang, F. Zhang, H. Lu, X. Hong, H. Jiang, Y. Wu, Y. Li, Hollow Zn/CoZIF particles derived from core-shell ZIF-67@ZIF-8 as selective catalyst for the semi-hydrogenation of acetylene, Angew. Chem. Int. Ed. 127 (2015) 11039–11043.

[26] J. Tang, R.R. Salunkhe, J. Liu, N.L. Torad, M. Imura, S. Furukawa, Y. Yamauchi, Thermal conversion of core-shell metal-organic frameworks: a new method for selectively functionalized nanoporous hybrid carbon, J. Am. Chem. Soc. 137 (2015) 1572–1580.

[27] X. Yang, S. Yuan, L. Zou, H. Drake, Y. Zhang, J. Qin, A. Alsalme, H.C. Zhou, One-step synthesis of hybrid core-shell metal-organic frameworks, Angew. Chem. Int. Ed. 130 (2018) 3991–3996.

[28] F.I. Pambudi, M.W. Anderson, M.P. Attfield, Unveiling the mechanism of lattice-mismatched crystal growth of a core-shell metal-organic framework, Chem. Sci. 10 (2019) 9571–9575.

[29] M.S. Yao, J.W. Xiu, Q.Q. Huang, W.H. Li, W.W. Wu, A.Q. Wu, L.A. Cao, W.H. Deng, G.E. Wang, G. Xu, Van der waals heterostructured MOF-on-MOF thin films: cascading functionality to realize advanced chemiresistive sensing, Angew. Chem. Int. Ed. 131 (2019) 15057–15061.

[30] Z. Wang, J. Liu, B. Lukose, Z. Gu, P.G. Weidler, H. Gliemann, T. Heine, C. Wöll, Nanoporous designer solids with huge lattice constant gradients: multiheteroepitaxy of metal-organic frameworks, Nano Lett. 14 (2014) 1526–1529.

[31] S. Choi, T. Kim, H. Ji, H.J. Lee, M. Oh, Isotropic and anisotropic growth of metal-organic framework (MOF) on MOF: logical inference on MOF structure based on growth behavior and morphological feature, J. Am. Chem. Soc. 138 (2016) 14434–14440.

[32] H.J. Lee, Y.J. Cho, W. Cho, M. Oh, Controlled isotropic or anisotropic nanoscale growth of coordination polymers: formation of hybrid coordination polymer particles, ACS Nano 7 (2013) 491–499.

[33] D. Wang, J. Zhou, R. Chen, R. Shi, C. Wang, J. Lu, G. Zhao, G. Xia, S. Zhou, Z. Liu, Core-shell metal-organic frameworks as Fe^{2+} suppliers for Fe^{2+}-mediated cancer therapy under multimodality imaging, Chem. Mater. 29 (2017) 3477–3489.

[34] D. Wang, J. Zhou, R. Shi, H. Wu, R. Chen, B. Duan, G. Xia, P. Xu, H. Wang, S. Zhou, Biodegradable core-shell dual-metal-organic-frameworks nanotheranostic agent for multiple imaging guided combination cancer therapy, Theranostics 7 (2017) 4605.

[35] G. Lee, S. Lee, S. Oh, D. Kim, M. Oh, Tip-to-middle anisotropic MOF-on-MOF growth with a structural adjustment, J. Am. Chem. Soc. 142 (2020) 3042–3049.

[36] C. Liu, Q. Sun, L. Lin, J. Wang, C. Zhang, C. Xia, T. Bao, J. Wan, R. Huang, J. Zou, Ternary MOF-on-MOF heterostructures with controllable architectural and compositional complexity via multiple selective assembly, Nat. Commun. 11 (2020) 1–8.

[37] Y. Gu, Yn Wu, L. Li, W. Chen, F. Li, S. Kitagawa, Controllable modular growth of hierarchical MOF-on-MOF architectures, Angew. Chem. Int. Ed. 129 (2017) 15864–15868.

[38] S. Kampouri, F.M. Ebrahim, M. Fumanal, M. Nord, P.A. Schouwink, R. Elzein, K. C. Stylianou, Enhanced visible-light-driven hydrogen production through MOF/MOF heterojunctions, ACS Appl. Mater. Interfaces 13 (2021) 14239–14247.

[39] P. Zhang, X.W. Lou, Design of heterostructured hollow photocatalysts for solar-to-chemical energy conversion, Adv. Mater. 31 (2019) 1900281.

[40] D. Dong, C. Yan, J. Huang, N. Lu, P. Wu, J. Wang, Z. Zhang, An electron-donating strategy to guide the construction of MOF photocatalysts toward co-catalyst-free highly efficient photocatalytic H_2 evolution, J. Mater. Chem. A 7 (2019) 24180–24185.

[41] S. Zhang, M. Du, Z. Xing, Z. Li, K. Pan, W. Zhou, Defect-rich and electron-rich mesoporous Ti-MOFs based NH_2-MIL-125(Ti)@$ZnIn_2S_4$/CdS hierarchical tandem heterojunctions with improved charge separation and enhanced solar-driven photocatalytic performance, Appl. Catal. B 262 (2020), 118202.

[42] X. Chen, Y. Cai, R. Liang, Y. Tao, W. Wang, J. Zhao, X. Chen, H. Li, D. Zhang, NH_2-UiO-66 (Zr) with fast electron transfer routes for breaking down nitric oxide via photocatalysis, Appl. Catal. B 267 (2020), 118687.

[43] S. Zhang, Y. Liu, P. Gu, R. Ma, T. Wen, G. Zhao, L. Li, Y. Ai, C. Hu, X. Wang, Enhanced photodegradation of toxic organic pollutants using dual-oxygen-doped porous g-C_3N_4: mechanism exploration from both experimental and DFT studies, Appl. Catal. B 248 (2019) 1–10.

[44] Y. Song, J. Tian, S. Gao, P. Shao, J. Qi, F. Cui, Photodegradation of sulfonamides by g-C_3N_4 under visible light irradiation: effectiveness, mechanism and pathways, Appl. Catal. B 210 (2017) 88–96.

[45] H. Alamgholiloo, N. Noroozi Pesyan, R. Mohammadi, S. Rostamnia, M. Shokouhimehr, Synergistic advanced oxidation process for the fast degradation of ciprofloxacin antibiotics using a GO/CuMOF-magnetic ternary nanocomposite, J. Environ. Chem. Eng. 9 (2021), 105486.

[46] B. Hashemzadeh, H. Alamgholiloo, N. Noroozi Pesyan, E. Asgari, A. Sheikhmohammadi, J. Yeganeh, H. Hashemzadeh, Degradation of ciprofloxacin using hematite/MOF nanocomposite as a heterogeneous fenton-like catalyst: a comparison of composite and core-shell structures, Chemosphere 281 (2021), 130970.

[47] H. Alamgholiloo, B. Hashemzadeh, N. Noroozi Pesyan, A. Sheikhmohammadi, E. Asgari, J. Yeganeh, H. Hashemzadeh, A facile strategy for designing core-shell nanocomposite of ZIF-67/Fe_3O_4: a novel insight into ciprofloxacin removal from wastewater, Process Saf. Environ. Prot. 147 (2021) 392–404.

[48] H. Alamgholiloo, S. Rostamnia, N. Noroozi Pesyan, Extended architectures constructed of thiourea-modified SBA-15 nanoreactor: a versatile new support for the fabrication of palladium pre-catalyst, Appl. Organomet. Chem. 34 (2020) 5452.

[49] S. Babaee, M. Zarei, H. Sepehrmansourie, M.A. Zolfigol, S. Rostamnia, Synthesis of metal-organic frameworks MIL-101(Cr)-NH_2 containing phosphorous acid functional groups: application for the synthesis of *N*-Amino-2-pyridone and pyrano [2, 3-*c*] pyrazole derivatives via a cooperative vinylogous anomeric-based oxidation, ACS Omega 5 (2020) 6240–6249.

[50] H. Sepehrmansouri, M. Zarei, M.A. Zolfigol, A.R. Moosavi-Zare, S. Rostamnia, S. Moradi, Multilinker phosphorous acid anchored En/MIL-100(Cr) as a novel nanoporous catalyst for the synthesis of new *N*-heterocyclic pyrimido [4, 5-*b*] quinolines, Mol. Catal. 481 (2020), 110303.

[51] H. Sepehrmansourie, M. Zarei, M.A. Zolfigol, S. Babaee, S. Rostamnia, Application of novel nanomagnetic metal-organic frameworks as a catalyst for the synthesis of new pyridines and 1, 4-dihydropyridines via a cooperative vinylogous anomeric based oxidation, Sci. Rep. 11 (2021) 1–15.

[52] S. Kalhor, M. Zarei, M.A. Zolfigol, H. Sepehrmansourie, D. Nematollahi, S. Alizadeh, H. Shi, J. Arjomandi, Anodic electrosynthesis of MIL-53 (Al)-*N* $(CH_2PO_3H_2)_2$ as a mesoporous catalyst for synthesis of novel (*N*-methyl-pyrrol)-pyrazolo [3, 4-*b*] pyridines via a cooperative vinylogous anomeric based oxidation, Sci. Rep. 11 (2021) 1–20.

[53] A.M. Naseri, M. Zarei, S. Alizadeh, S. Babaee, M.A. Zolfigol, D. Nematollahi, J. Arjomandi, H. Shi, Synthesis and application of [Zr-UiO-66-PDC-SO_3H]Cl MOFs

to the preparation of dicyanomethylene pyridines via chemical and electrochemical methods, Sci. Rep. 11 (2021) 1–19.
[54] R. Mohammadi, H. Alamgholiloo, B. Gholipour, S. Rostamnia, S. Khaksar, M. Farajzadeh, M. Shokouhimehr, Visible-light-driven photocatalytic activity of ZnO/g-C_3N_4 heterojunction for the green synthesis of biologically interest small molecules of thiazolidinones, J. Photochem. Photobiol. A 402 (2020), 112786.
[55] R. Mohammadi, B. Gholipour, H. Alamgholiloo, S. Rostamnia, H. Mohtasham, A. Zonouzi, S. Ramakrishna, M. Shokouhimehr, Nano-construction of CuO nanorods decorated with g-C_3N_4 nanosheets (CuO/g-C_3N_4-NS) as a superb colloidal nanocatalyst for liquid phase CH conversion of aldehydes to amides, J. Mol. Liq. 334 (2021), 116063.
[56] H. Zhu, R. Li, G. Liu, Y. Pan, J. Li, Z. Wang, Y. Guo, G. Liu, W. Jin, Efficient separation of methanol/dimethyl carbonate mixtures by UiO-66 MOF incorporated chitosan mixed-matrix membrane, J. Membr. Sci. 652 (2022), 120473.
[57] M. Dan-Hardi, C. Serre, T. Frot, L. Rozes, G. Maurin, C. Sanchez, G. Férey, A new photoactive crystalline highly porous titanium (IV) dicarboxylate, J. Am. Chem. Soc. 131 (2009) 10857–10859.
[58] S. Yu, J. Li, Y. Zhang, M. Li, F. Dong, T. Zhang, H. Huang, Local spatial charge separation and proton activation induced by surface hydroxylation promoting photocatalytic hydrogen evolution of polymeric carbon nitride, Nano Energy 50 (2018) 383–392.
[59] X. Zhang, Z. Chen, Y. Luo, X. Han, Q. Jiang, T. Zhou, H. Yang, J. Hu, Construction of NH_2-MIL-125(Ti)/CdS Z-scheme heterojunction for efficient photocatalytic H_2 evolution, J. Hazard. Mater. 405 (2021), 124128.
[60] H. Li, H. Chu, X. Ma, G. Wang, F. Liu, M. Guo, W. Lu, S. Zhou, M. Yu, Efficient heterogeneous acid synthesis and stability enhancement of UiO-66 impregnated with ammonium sulfate for biodiesel production, Chem. Eng. J. 408 (2021), 127277.
[61] J. Zhu, P. Xiao, H. Li, S.A. Carabineiro, Graphitic carbon nitride: synthesis, properties, and applications in catalysis, ACS Appl. Mater. Interfaces 6 (2014) 16449–16465.
[62] K. Chakarova, I. Strauss, M. Mihaylov, N. Drenchev, K. Hadjiivanov, Evolution of acid and basic sites in UiO-66 and UiO-66-NH_2 metal-organic frameworks: FTIR study by probe molecules, Microporous Mesoporous Mater. 281 (2019) 110–122.
[63] D. Zhang, B. Mao, D. Li, Y. Liu, F. Li, W. Dong, T. Jiang, W. Shi, 0D/2D Z-scheme heterojunctions of Zn-$AgIn_5S_8$ QDs/α-Fe_2O_3 nanosheets for efficient visible-light-driven hydrogen production, Chem. Eng. J. 417 (2021), 128275.
[64] X.-M. Cheng, X.-Y. Dao, S.-Q. Wang, J. Zhao, W.-Y. Sun, Enhanced photocatalytic CO_2 reduction activity over NH_2-MIL-125(Ti) by facet regulation, ACS Catal. 11 (2020) 650–658.
[65] Y. Wang, S. Zhang, Y. Zhao, J. Bedia, J. Rodriguez, C. Belver, UiO-66-based metal organic frameworks for the photodegradation of acetaminophen under simulated solar irradiation, J. Environ. Chem. Eng. 9 (2021), 106087.
[66] R. Keyikoglu, A. Khataee, H. Lin, Y. Orooji, Vanadium (V)-doped ZnFe LDH for enhanced sonocatalytic degradation of pymetrozine, Chem. Eng. J. 434 (2022), 134730.
[67] A. Wang, H. Wang, H. Deng, S. Wang, W. Shi, Z. Yi, R. Qiu, K. Yan, Controllable synthesis of mesoporous manganese oxide microsphere efficient for photo-Fenton-like removal of fluoroquinolone antibiotics, Appl. Catal. B 248 (2019) 298–308.
[68] J. Hand, K. Gebhart, B. Schichtel, W. Malm, Increasing trends in wintertime particulate sulfate and nitrate ion concentrations in the Great Plains of the United States (2000–2010), Atmos. Environ. 55 (2012) 107–110.
[69] D.E. Santiago, J. Araña, O. González-Díaz, M. Alemán-Dominguez, A.C. Acosta-Dacal, C. Fernandez-Rodríguez, J. Pérez-Peña, J.M. Doña-Rodríguez, Effect of inorganic ions on the photocatalytic treatment of agro-industrial wastewaters containing imazalil, Appl. Catal. B 156 (2014) 284–292.
[70] X. Li, Y. Qiu, Z. Zhu, T. Chen, H. Zhang, D. Yin, Construction of magnetically separable dual Z-scheme g-C_3N_4/α-Fe_2O_3/Bi_3TaO_7 photocatalyst for effective degradation of ciprofloxacin under visible light, Chem. Eng. J. 440 (2022), 135840.
[71] L. Shi, X. Zou, T. Wang, D. Wang, M. Fan, Z. Gong, Sunlight photocatalytic degradation of ofloxacin using UiO-66/wood composite photocatalysts, Chin. Chem. Lett. 33 (2022) 442–446.
[72] D. Zhang, J. Qi, H. Ji, S. Li, L. Chen, T. Huang, C. Xu, X. Chen, W. Liu, Photocatalytic degradation of ofloxacin by perovskite-type $NaNbO_3$ nanorods modified g-C_3N_4 heterojunction under simulated solar light: theoretical calculation, ofloxacin degradation pathways and toxicity evolution, Chem. Eng. J. 400 (2020), 125918.